

Pearling instability of nanoscale fluid flow confined to a chemical channel

J. Koplik and T. S. Lo

*Benjamin Levich Institute and Department of Physics,
City College of the City University of New York, New York, NY 10031*

M. Rauscher and S. Dietrich

*Max-Planck-Institut für Metallforschung, Heisenbergstr. 3, 70569 Stuttgart, Germany, and
Institut für Theoretische und Angewandte Physik,
Universität Stuttgart, Pfaffenwaldring 57, 70569 Stuttgart, Germany*

(Dated: November 10, 2018)

We investigate the flow of a nano-scale incompressible ridge of low-volatility liquid along a “chemical channel”: a long, straight, and completely wetting stripe embedded in a planar substrate, and sandwiched between two extended less wetting solid regions. Molecular dynamics simulations, a simple long-wavelength approximation, and a full stability analysis based on the Stokes equations are used, and give qualitatively consistent results. While thin liquid ridges are stable both statically and during flow, a (linear) pearling instability develops if the thickness of the ridge exceeds half of the width of the channel. In the flowing case periodic bulges propagate along the channel and subsequently merge due to nonlinear effects. However, the ridge does not break up even when the flow is unstable, and the qualitative behavior is unchanged even when the fluid can spill over onto a partially wetting exterior solid region.

I. INTRODUCTION

In recent years substantial efforts have been invested in miniaturizing chemical processes by building microfluidic systems. The “lab on a chip” concept integrates a great variety of chemical and physical processes into a single device [1, 2, 3] in a similar way as an integrated circuit incorporates many electronic devices into a single chip. These microfluidic devices do not only allow for cheap mass production but they can operate with much smaller quantities of reactants and reaction products than standard laboratory equipments. Even though most available microfluidic devices today have micron sized channels, further miniaturization is leading towards the nano-scale.

There are two main lines of development for microfluidic systems. The first one encompasses systems with closed channels, essentially microfabricated tubes. However, closed channel systems have the disadvantage that they can be easily clogged by solute particles such as colloids or large bio-polymers.

The second type consists of systems which are open with a free liquid-vapor interface, where the fluid is confined laterally not by geometrical but by chemical walls. The idea is that the liquid will be guided by lyophilic stripes on an otherwise lyophobic substrate [4, 5, 6]. The substrate surfaces can be structured chemically by printing or photographic techniques. All these techniques are confined to two dimensions.

While liquid flow in closed channel systems can be pumped by applying a pressure difference between the inlet and the outlet, the liquid-vapor interface of an open system would yield to the pressure (like a very soft rubber tube) and droplets would form. Furthermore, upon pumping flow directions in interconnected open channel systems would be difficult to predict because small droplets may or may not inflate into larger ones, depending on details of the channel geometry and the filling state. However, there are a number of alternative ways to drive a liquid through a chemical channel. The most obvious one is to use inertia to drive the flow, e.g., centrifugal forces or gravity, as occurs when a liquid film flows down an inclined plane. For films with thicknesses in the nanometer range one needs stronger accelerations in order to achieve a decent throughput. These can be realized most conveniently on a rotating disc (e.g., a spin coater or a centrifuge). Electric forces are also commonly used in order to drive flows in small channels, e.g., by using the electro-osmotic effect which, however, only works for liquids containing ions. Since water is the most interesting liquid for biological applications, this is not a serious restriction. Depending on the wall potential, a charged layer a few Å in thickness forms and an electric field applied parallel to the substrate will set the liquid in this layer in motion. While the electro-osmotic effect drives the liquid molecules at the substrate, the Marangoni effect drives the molecules at the liquid-vapor interface. The origin of the Marangoni forces are gradients in surface tension which arise from temperature gradients or from gradients in surfactant concentrations. The fourth method to cause flow in a chemical channel is wicking, i.e., the sucking of a droplet into a chemical channel by capillary forces.

Here we consider inertial driving of the liquid, which is one of the most promising methods to generate flow in open microfluidic devices. Marangoni forces could be induced easily by local heating of the liquid, but for volatile fluids like water this will lead to enhanced and undesirable evaporation. Wicking is slow for longer channels and ceases to act as a driving force once the channel is filled. In principle, electrical forcing has the advantage that the direction of the force can be controlled on very small scales, but the required fields are high and might lead to electrolysis. In

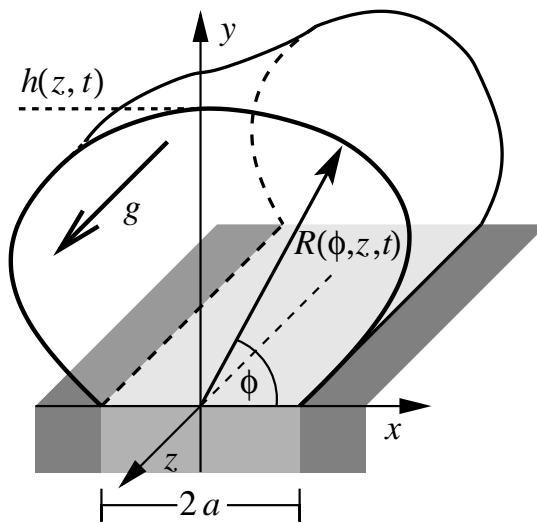


FIG. 1: A liquid ridge on a chemical wetting stripe of width $2a$ embedded in a solid substrate, which is non-wetting. Gravity or inertial forces act on the liquid in the direction parallel to the z -axis. The liquid-vapor interface is parameterized in cylindrical coordinates as $r = R(\phi, z, t)$, and the local height $h(z, t) = R(\pi/2, z, t)$.

contrast, inertial driving can be realized easily by centrifugal forces and does not affect the liquid sample.

Our focus in this paper is the stability and robustness of one-dimensional channel flow (i.e., flow in a straight channel) with inertial forcing aligned with the channel direction. The flow geometry is sketched in Fig. 1. In the absence of forcing, a chemical channel filled homogeneously by a non-volatile liquid of fixed volume is unstable with respect to droplet formation when the contact angle with the triple-line pinned at the channel edge exceeds 90° [7, 8]. This pearling instability is surface tension driven and similar to the Rayleigh-Plateau instability. The resulting drop shapes have been studied extensively in Ref. [9]. Of particular interest is the question of spilling onto the lyophobic substrate, which can lead to cross-talk between neighboring channels. In the force-free case this happens for large droplets on chemical stripes on a partially wetting embedding substrate.

In Sec. II we describe the formulation of the molecular dynamics (MD) simulations for flow on a chemical channel and discuss the special case of unidirectional flow quantitatively. In Sec. III we discuss the appearance of pearling instabilities in channel flows and, in particular, we study the influence of the liquid ridge height (effectively, the channel depth) and of the wetting properties of the surrounding substrate on the stability of the liquid ridge. The full linear stability analysis of a Stokes flow in Sec. IV as well as the hydrodynamic long-wavelength approximation developed in Sec. V are in qualitative agreement with the MD simulations. We discuss the results in Sec. VI.

II. MOLECULAR DYNAMICS SIMULATIONS

The MD simulations carried out here employ standard techniques [10, 11] and a simple molecular model for a non-polar liquid in contact with a thermally-fluctuating solid [12, 13], based on atoms interacting via an adjustable Lennard-Jones potential

$$V_{\text{LJ}}(r) = 4\epsilon \left[\left(\frac{r}{\sigma}\right)^{-12} - c_{ij} \left(\frac{r}{\sigma}\right)^{-6} \right]. \quad (1)$$

The interaction is cut off at $r_c = 2.5\sigma$, and shifted by a linear term so that the force vanishes smoothly there. In this section we employ so-called “MD units” derived from this potential, with the atomic core size σ as the unit of length, the potential well depth ϵ as the unit of energy, and $\tau \equiv \sigma(m/\epsilon)^{1/2}$ as the unit of time t , where m is the mass of the liquid atoms. We simulate a generic non-polar liquid rather than any particular laboratory material, but typical numerical values are $\sigma \approx 0.3$ nm, $\epsilon/k_B \approx 140$ K, and $\tau \approx 2$ ps. A monatomic Lennard-Jones fluid exhibits a high vapor pressure and a very broad liquid-vapor interface. These are inconvenient properties in the present context and are ameliorated by using a FENE potential

$$V_F(r) = -\frac{1}{2} k_F r_0^2 \ln \left(1 - \frac{r^2}{r_0^2} \right) \quad (2)$$

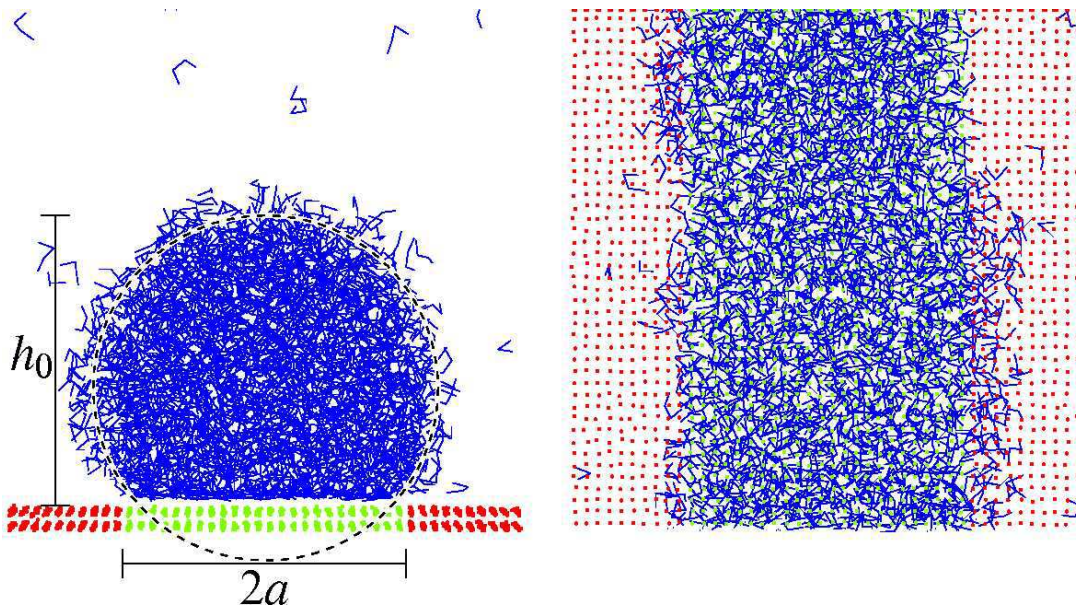


FIG. 2: Snapshot of a typical initial molecular configuration. The left and right views are along and top down on the stripe, respectively. The liquid molecules are depicted as the three “bonds” joining the four atoms, while substrate atoms with wetting ($c_{LS} = 1$) and non-wetting ($c_{LS} = 0$) properties are light green and dark red dots, respectively. The average spacing between solid atoms is 0.78σ . The liquid ridge has a circular cross section (as indicated by the dashed circle) and a height h_0 (at which the density attains half its value in the center), which depends on the liquid volume and the stripe width $2a$.

to group the atoms into freely-jointed chain molecules which are four atoms in length. The numerical values of the constants in V_F are $k_F = 30\epsilon/\sigma^2$ and $r_0 = 1.5\sigma$, following Ref. [14]. This leads to a significant reduction of the vapor pressure and thus yields a liquid of low volatility. The solid atoms are tethered to two layers of fcc lattice sites $\{\mathbf{r}_{0i}\}$ with lattice constant 1.55σ using a stiff spring

$$V_S(\mathbf{r}_i) = \frac{1}{2} k_S (\mathbf{r}_i - \mathbf{r}_{0i})^2 \quad i = 1, \dots, n_S \quad (3)$$

with spring constant $k_S = 100\epsilon/\sigma^2$, allowing the liquid and solid to exchange energy and momentum. The substrate surface has a (100) crystallographic orientation. The solid atom mass is chosen as $100m$, so as to have approximately the same oscillation frequency as the LJ interactions and a common time step in the numerical integration. During the simulations, a Nosé-Hoover thermostat maintains a constant temperature $1.0\epsilon/k_B$. Under these conditions, the fluid condenses into a liquid of number density $0.79\sigma^{-3}$, in equilibrium with a modest amount of vapor.

The coefficient c_{ij} in Eq. (1) is used to vary the strength of the attractive interaction between atomic species i and j . The intra-liquid coefficient has the (standard) value $c_{LL} = 1.0$. With the other modeling choices and parameter values given above, the liquid wets the solid completely, partially, and not at all for the choices $c_{LS} = 1.0, 0.75,$ and 0.0 , respectively. The corresponding contact angles for a drop on a homogeneous solid with these values of c_{LS} are 0° , approximately 90° , and 180° , respectively. In the latter case and in the absence of gravity, a drop actually drifts off the surface. The surface tension of the liquid is found from a standard simulation of a slab of liquid coexisting with vapor to be $\gamma = 0.46\epsilon/\sigma^2$, and the liquid viscosity is obtained from a separate simulation of Couette flow as $\eta = 3.60m/(\sigma\tau)$.

A snapshot of the basic simulated configuration is shown in Fig. 2, i.e., the individual atoms in a liquid ridge on a wetting stripe for a case where the exterior of the channel is completely non-wetting. The left figure shows an end-on view (parallel to the stripe) and the right figure a section of the top view. Note that the interaction does confine the liquid to the wetting region, and that the interface strongly fluctuates. In this and all other simulations, we apply periodic boundary conditions in the plane of the substrate in order to avoid end effects. To construct the atomic configurations, we place atoms on the sites of a cylindrical section of a fcc lattice and allow them to move under the action of the LJ and FENE potentials given above until the atomic positions become disordered and the internal energy stabilizes. This configuration does not correspond to global thermodynamic equilibrium because, as we shall see, a uniformly shaped liquid ridge is hydrodynamically unstable; however, this configuration can be described in terms of a local equilibrium. The resulting cylinder of liquid is translated to lie just above and parallel to the wetting stripe of a solid substrate which has been independently allowed to reach local equilibrium, so that the liquid is

attracted towards the substrate and adjusts itself to form an irregular circular ridge with height h_0 as shown in Fig. 2. During the course of the equilibration process, lasting typically several hundred τ , the liquid surface fluctuates at a 5% level in an apparently random manner. Systematic changes in the shape of the ridge occur only on longer time scales.

In order to simulate liquid flow, we apply a uniform force $mg\mathbf{e}_z$ to each liquid atom, where the axis of the stripe is the z -direction (see Fig. 1). The results presented in this paper involve values $g = 0.01\text{--}0.05\sigma/\tau^2$, and the corresponding Reynolds numbers, based on the observed mean flow velocities and the height of the liquid ridge, are $\text{Re} = 0.1\text{--}10.0$. Smaller values of g are perhaps more realistic but require longer computations for the flow and for any changes in interfacial shape to develop. In any case, these low-Reynolds number simulations are in the linear regime where phenomena simply scale in time with $1/g$. At higher g , the liquid is often driven off the substrate.

In order to relate the MD simulation results to macroscopic hydrodynamics, we consider the special case in which the liquid occupies just half of a cylinder with a 90° contact angle, with initial height $h_0 = a$. As discussed below in Sects. IV and V, this case is neutrally stable with respect to changes in interface shape and the shape of the ridge does not change significantly over the time of the simulation. Furthermore, this case may be directly compared (over moderate time intervals) with solutions of the Navier-Stokes (NS) equations for unidirectional flow parallel to the stripe axis. Furthermore, the unidirectional NS flow field may be computed in an almost closed form by a Fourier series method (see Sec. IV for details). In Fig. 3 we show the liquid density, the axial velocity field, and the r - z component of the shear stress, as obtained from the analytic solution and from the MD simulations, at the same resolution. (The explicit analytic form of the shear stress can be obtained from the formulas in Sec. IV and the MD counterpart is the Irving-Kirkwood expression [10].) In order to obtain these fields from the simulations, the flow domain in the x - y plane was divided into square bins of size $\sigma \times \sigma$, and the appropriate quantity in each bin was averaged both over time (2000τ) and the length of the system in z -direction (517σ). A larger averaging time interval was impractical due to the eventual development of systematic interfacial fluctuations, while smaller sampling bins lead to excessive noise in the stress (and wall-induced oscillations in the liquid density near the solid [12]). The jaggedness in the NS figures results from the relatively small number of bins (31×16) occupied by the liquid, while that in the MD figures incorporates thermal fluctuations as well.

The first point to note is that the MD liquid-vapor interface is rather diffuse, corresponding to a width of about 7 sampling bins. This feature is not easily accounted for in the NS calculation, so that close agreement should not be expected. Secondly, we see that while the shear stress values are in qualitative agreement both in shape and magnitude and the velocity fields have the same shape, the velocity values differ by almost a factor of 2. This comparison depends critically on the value chosen for the liquid ridge height in the NS calculations: a larger height increases the velocity values and decreases the stress, so that a different choice could make both agree to 50%. Here, in computing the NS flow field, we selected the numerical value of the height h_0 based on the reasonable but arbitrary definition as the point where the MD density dropped to half the value at the center of the ridge (see Figs. 1 and 2). The fact that the MD velocities are larger may result from the fact the free surface region of the ridge exhibits a transition between liquid and gaseous phases and time-averaged velocities in the latter are larger. In any case, the degree of agreement between MD and NS hydrodynamics is worse than in similar comparisons where the liquid is completely confined by walls [12], which we attribute to the diffuse top boundary of the liquid. A final remark is that the (thermal) fluctuations in the MD results are largest for the stress, moderate for the velocity, and almost invisible in the density. The reason is that the stress computation involves the intermolecular force, which is a rapidly varying function of atomic separation, while the velocities result from an integration over the force, which provides some smoothing. The density follows from the atomic positions, which are a further integral of the velocity, and is thus still smoother.

III. PEARLING INSTABILITIES

Turning now to the systematic study of pearling instabilities, we have conducted a number of simulations in which we explore the effects of several operating parameters. For a fixed number of liquid atoms (128,000, or 32,000 molecules) we vary

- filling: the number of liquid particles per stripe length on the wetting stripe. In practice, we choose different widths for the solid wetting stripe, and since the liquid is effectively pinned to the edges of the stripe, it adjusts its height and contact angle such that a circular cross section emerges.
- wetting: the region exterior to the completely wetting stripe can be either completely non-wetting (i.e., drying) or partially wetting. In the former case the liquid is confined to the stripe and does not contact the exterior, but in the latter case it can spill over the edges.
- forcing: the value of the acceleration g .

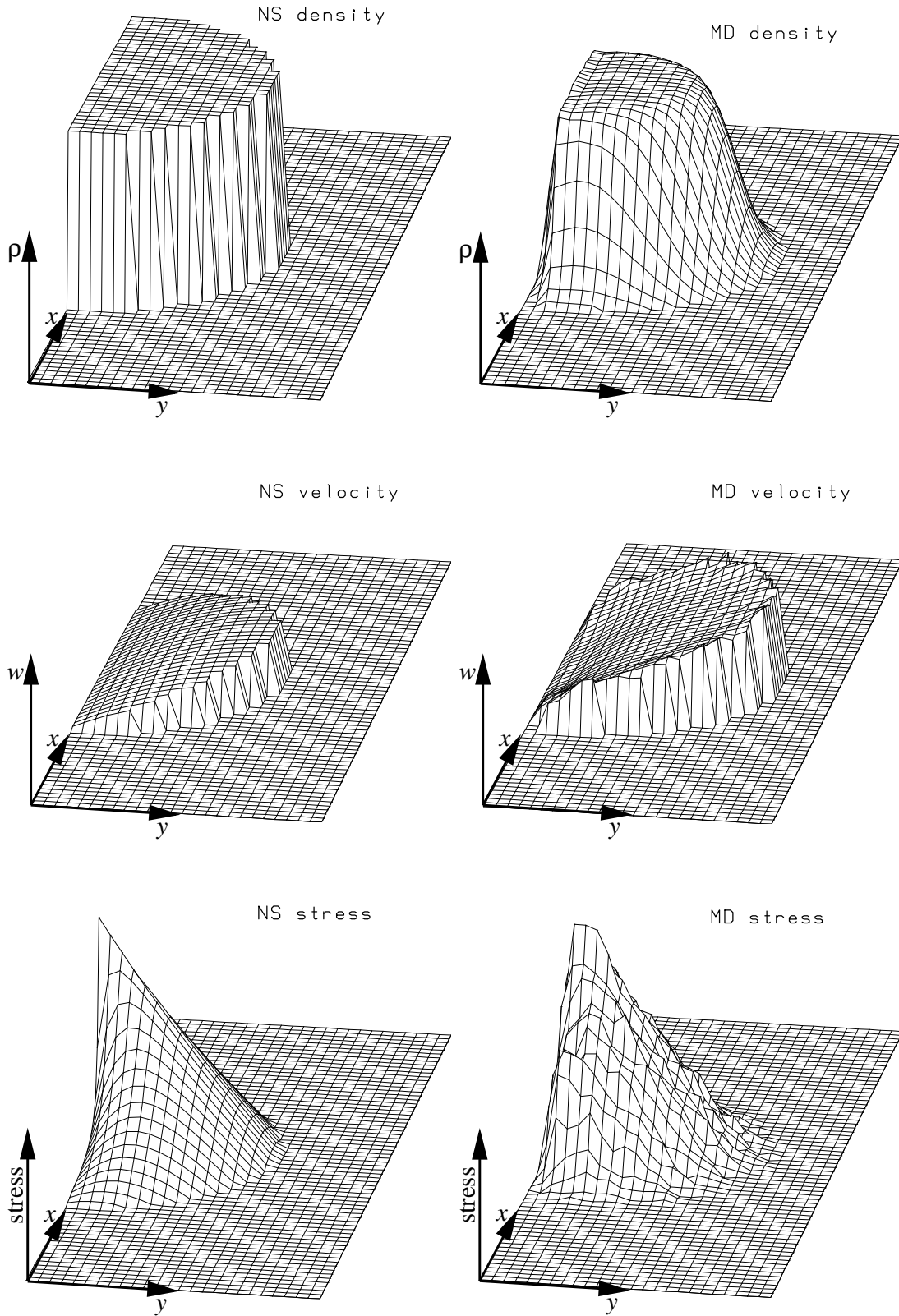


FIG. 3: Comparison of the density, axial velocity and r - z shear stress fields in a liquid ridge with initial height $h_0 = a = 16\sigma$ for unidirectional flow with $g = 0.01$ (see Fig. 1 for the coordinate definitions). In each frame of the figure the base is the x - y plane, with the substrate (not shown) to the left. The height of the surface represents the value of the field depicted there, and the grid spacing is σ . In the density plots, the plateau height, representing the central liquid density, is $0.79 \sigma^{-3}$. In the Navier-Stokes (NS) velocity and stress plots, the maximum values are $0.225 \sigma/\tau$ and $0.107 m/(\sigma\tau^2)$, respectively, and for each field the same scales and units are used for NS and MD. The MD fields are set to zero in bins (of size $\sigma \times \sigma$) where the density is below $0.01 \sigma^{-3}$. The exterior of the substrate is nonwetting ($c_{LS} = 0$) whereas the stripe is wetting ($c_{LS} = 1$).

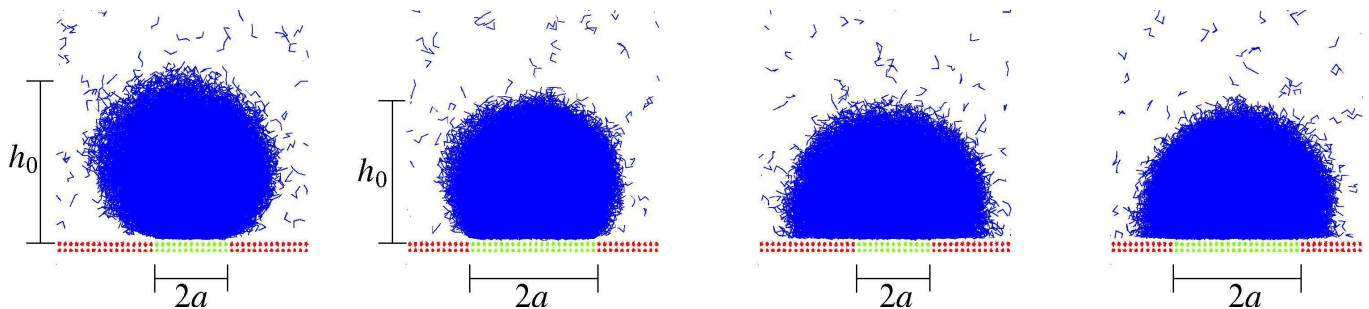


FIG. 4: Head on view along the z -axis of the initial configuration of the cases simulated. From left to right: non-wetting ($c_{LS} = 0$) exterior and narrow wetting ($c_{LS} = 1$) stripe with $h_0/a = 4.0$; non-wetting exterior and wide wetting stripe with $h_0/a = 2.2$; partially wetting ($c_{LS} = 0.75$) exterior and narrow wetting stripe with $h_0/a = 3.1$; partially wetting exterior and wide wetting stripe with $h_0/a = 1.7$. The number of molecules per channel length is the same in all cases.

- length: simulations have been carried out using one-half and one-quarter of the stripe length and, correspondingly, of the number of atoms, but with identical cross-sectional shapes. This allows one to examine the wavelength selection if pearling develops.

At early times before any instability has appeared, Fig. 4 gives head-on snapshots of the cross sectional shape of the liquid for the two choices of filling and two choices of wetting considered in this paper. In the two cases of a completely non-wetting exterior solid shown in Fig 4, the key geometric parameters for the Stokes equation analysis below are the wetting stripe width $2a$ and the initial liquid height h_0 . The case of a narrow stripe corresponds to a width $2a = 10.6\sigma$ and a height-to-half-width ratio $h_0/a = 4.0$, while the case of a wide stripe corresponds to a width $2a = 17.1\sigma$ with $h_0/a = 2.2$. The maximum system length considered here is 547σ with 128,000 atoms.

First we consider the case of no forcing. If a static liquid ridge of uniform cross-sectional shape with contact lines pinned at the chemical steps (ridges with a mobile contact line are always unstable [7]) is sufficiently long and thick, it is expected to be unstable to the formation of bulges, as shown by various authors [5, 7, 9, 15]. This instability is driven by surface tension, and is closely related to the well-known Rayleigh-Plateau instability of a liquid cylinder, which reduces its surface area under long-wavelength perturbations of its radius, eventually breaking up into spheres. Here, the qualification “thick” means that the contact angle must be larger than 90° or equivalently, because the liquid cross section in equilibrium must be an arc of a circle, the initial height must be greater than half the width of the wetting region, i.e., $h_0 > a$.

This static instability appears naturally in MD simulations. In Fig. 5 we show an example where the initial height was 2.0 times the stripe width, and the system had 64,000 atoms and half the maximum length studied by us. In this and in subsequent figures, instead of individual atoms we plot the median liquid interface, defined as the surface on which the liquid density averaged over a 50τ interval falls to half of the value at the center. A second simulation with initial height $h_0 = a$ was stable over the same time interval, showing continued random fluctuations in shape but no systematic evolution. Because the liquid is strongly attracted to the wetting region of the substrate, the pearls (with a characteristic wavelength) arising from the instability remain connected by thin liquid films over the duration of the simulation. Neither the simulations, nor the linear stability analyses below, can reliably predict the ultimate asymptotic state and we cannot determine whether the liquid pearls remain connected or not in the true asymptotic sense $t \rightarrow \infty$, i.e., in thermal equilibrium. Note that the Surface Evolver software used in [5, 9, 15] does not incorporate the substrate potential as such and cannot address the issue of adsorbed films of molecular thicknesses. This could be resolved by density functional techniques combined with a constraint for the liquid volume; we regard it as likely that the pearls remain connected by thin liquid bridges. In the simpler case of the pure Rayleigh-Plateau instability, i.e., in the absence of a substrate, MD simulations similar to those described here are in rough agreement with theoretical predictions of the breakup time; see Refs. [16, 17].

The behavior of the same system when driven with an acceleration $g = 0.01$ is shown in Fig. 6 for the same initial shape. Also in this case pearls form, with the same initial wavelength as in the unforced case, and then propagate downstream with the moving liquid. While initially the deviations from the uniform thickness of the ridge are periodic and have the same velocity, as they develop to finite amplitude they presumably interact nonlinearly and acquire different velocities, and eventually merge into pairs until one moving pearl survives. If the length of the system is half as long, initially only two pearls are present, which eventually merge into one; with one quarter of the length, one pearl appears and it simply grows and propagates. If the simulation is repeated with g increased to 0.025, the same instability scenario is present (see Fig. 7) but the structure develops more rapidly, the pearls propagate at a higher velocity, and mergers occur sooner. At still higher values of acceleration, in the inertial regime with $Re > 1$,

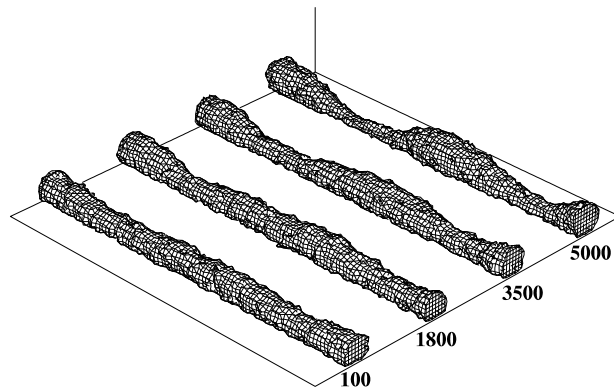


FIG. 5: Instability of a static liquid ridge with $h_0/a = 4.0$ in the nonwetting-narrow case (see Fig. 4). The sequence runs from left to right, showing the median interface position at the times indicated. The stripe length is 273.6σ and the vertical axis at the rear of the figure has a height of 51.3σ .

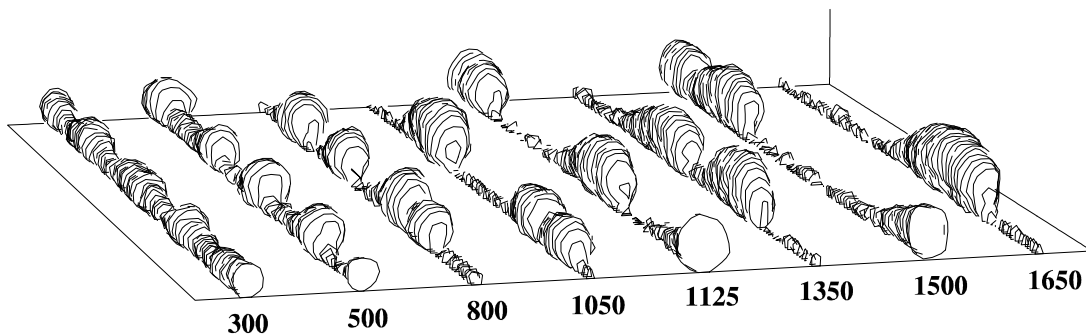


FIG. 6: Time evolution of the instability of a driven liquid ridge with the same aspect ratio and substrate properties as in Fig. 5 (i.e., $h_0/a = 4.0$) but with twice the system size driven at $g = 0.01$, showing propagating pearls and their merger. The forcing is along the channel from back to front, and the vertical axis at the rear of the figure has a height of 51.3σ .

the liquid tends to assume very irregular shapes and may even lose contact with the wetting stripe.

Somewhat surprisingly, the case that the embedding substrate exhibits partial wetting shows an identical qualitative behavior in terms of pearl formation, motion and merger, with only numerical differences in growth rate, wavelength, and velocity. Generally speaking, in these cases the motion is slower because the liquid spills over laterally and tends to be closer to the solid substrate, because the exterior part of the substrate is more attractive than in the previous case. The same number of pearls appear initially but require a longer time to develop and to subsequently merge. An example is shown in Fig. 8 for the case of a wide stripe of width $2a = 17.1\sigma$ at $g = 0.01$, and the principal difference from the corresponding results for a non-wetting exterior is the longer time scale. The corresponding top

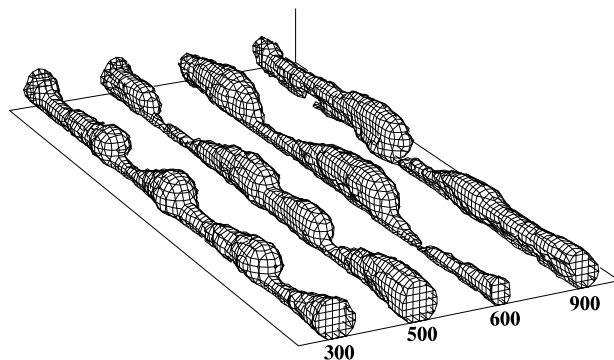


FIG. 7: The same system as in Fig. 6 but driven at a higher acceleration $g = 0.025$. Note the difference in time scale for the merging of the pearls. The vertical axis at the rear of the figure has a height of 51.3σ .

		wide: $h_0/a = 2.2$		narrow: $h_0/a = 4$	
		$g = 0.01$	$g = 0.025$	$g = 0.01$	$g = 0.025$
$T = 1/\omega_R$	MD	400	100-200	200	100
	LW	319	319	113	113
	NS	400	229	155	89
λ^*	MD	137	137	137	137
	LW	168	168	152	152
	NS	107	134	67	83
v	MD	0.59	1.46	0.99	1.51
	LW	0.46	1.15	1.06	2.65
	NS	0.53	0.67	0.86	1.1

TABLE I: Comparison of MD simulation, long wavelength (LW) approximation, and Navier-Stokes (NS) equations stability analysis, for four cases with a non-wetting exterior substrate. Two stripe widths (wide, $h_0/a = 2.2$, and narrow, $h_0/a = 4$) and two accelerations g were considered. T is a rough estimate of the time at which pearls start to become observable in the MD simulations, which is compared to ω_R^{-1} , the inverse of the real part of the instability growth rate. λ^* and v are the distance between the centers of neighboring pearls and their velocity, respectively.

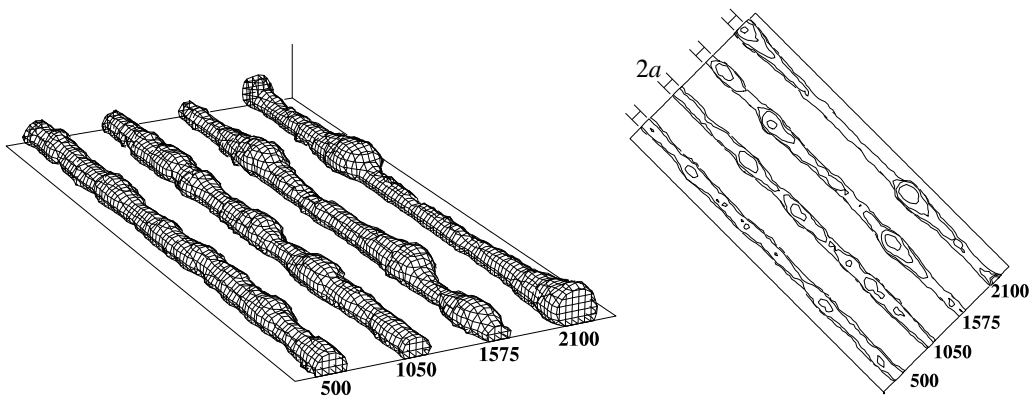


FIG. 8: Spatio-temporal effects due to a partially-wetting ($c_{LS} = 0.75$) exterior solid for a wide wetting stripe ($h_0/a = 2.1$) at $g = 0.01$. Left: perspective view, right: top view. The vertical axis at the rear of the left figure has a height of 51.3σ , and the contours in the right figure are lines of constant height. The scale bars indicate the width $2a$ of the wetting stripe.

views demonstrate that the lateral contact line formed by the liquid on the exterior solid tends to move outward near a pearl, but it never deviates very far from the edge of the stripe.

A summary of the numerical results for the onset time of the instability, its initial wavelength, and the pearl velocity for the cases with a non-wetting exterior substrate is given in Table I in the rows labeled MD, while the other entries are obtained from the stability analyses given below. In the table, the “MD” numbers assigned to the instability are rough estimates obtained by visual inspection. The onset time T is the time elapsed after the application of the forcing when a recognizable periodic disturbance (amplitude roughly 10% of h_0) appears in a side view of the liquid ridge. The wavelength is the average spacing between crests in the pattern, and the velocity is obtained from the displacement of the crests of the pearls at successive times. The numerical entries for the two analytic calculations are the values for the most unstable mode in each case. The situations involving a partially wetting exterior substrate present a rather more difficult stability problem, because in that case the lateral sides of the liquid ridge are mobile instead of being pinned at the stripe edges. We have not undertaken this stability analysis.

Of course, it would be preferable to compare MD and continuum results in terms of the time dependence of individual Fourier components of the deviation from a uniform axial shape. But in practice two difficulties prevent this analysis. First, on the atomic scale σ , the simulated liquid ridge exhibits a diffuse interfacial region, so that a prescription is needed to define a unique liquid-vapor interface. Second, independent of how the interface is defined, it undergoes capillary wave-like thermal fluctuations which can obscure the relevant signal. The procedure we tried was to choose equally spaced time intervals, to divide the liquid ridge into slices of constant-thickness along the flow axis, and at each time to count the number of atoms in each bin. Assuming that the number of atoms in each bin is proportional

to the cross-sectional area at that position z , and that locally the interface is an arc of a circle, geometry gives the local height $h(z, t)$ (see, c.f., Eq. (26)). The power spectrum of h is obtained by a fast Fourier transform, from which the time evolution of individual Fourier modes follows. If these modes had displayed an exponential growth at early times, a precise comparison with a stability analysis would be possible. However, we did not observe any systematic behavior of the modal growth rates: some increase with time but not exponentially over any appreciable time interval, while others simply vary in an irregular manner due to thermal fluctuations. In contrast, a recent MD calculation of the Rayleigh-Taylor instability in a two-liquid system was able to relate the interfacial shape to the growth of distinct Fourier modes [18]. The presence of the second liquid sharpens the interface and suppresses thermal fluctuations, allowing one to make closer contact with the spectral analysis.

Finally, we consider the effects of the pearling instability on liquid transport. One effect of pearl formation is to cause a net displacement of fluid molecules away from the substrate where they are partially bound by the substrate atoms providing a wetting condition, so that the mean velocity and the flux should increase as the instability grows. From a continuum point of view, the equivalent statement is that pearling moves the liquid further away from that part of the boundary on which the no-slip condition applies. In fact, as a function of time we observe a roughly linear increase of the mean *axial* velocity $\langle w \rangle$ (averaged over the whole liquid ridge) as shown for one example in Fig. 9. The velocities with which the pearls move are comparable to the mean flow velocities in each case. In view of the approximate way in which the pearl velocities are determined, i.e., by monitoring the position of the crests at regular intervals in time, it is difficult to obtain a more precise statement. At longer times, the mean velocity oscillates around the maximum value in Fig. 9 reflecting shape adjustments of the surviving pearl. Since in this case $\text{Re} = 0.1$, the roughly linear increase of $\langle w \rangle$ with time can be attributed to shape changes rather than to inertia.

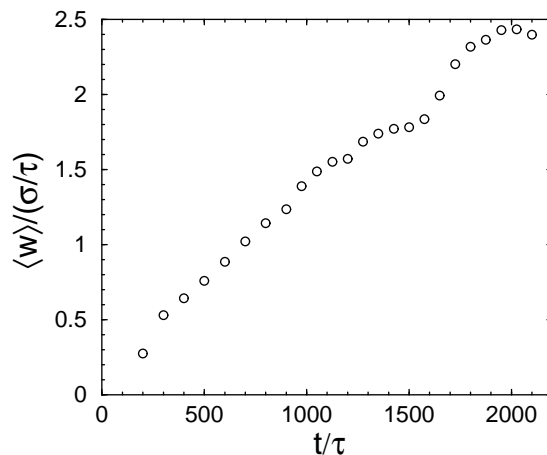


FIG. 9: Mean axial velocity $\langle w \rangle$ vs. time for the case of a narrow wetting stripe embedded into a non-wetting substrate ($h_0/a = 4$) as shown in Fig. 6 driven at $g = 0.01$.

IV. STABILITY ANALYSIS

In this section, we analyze the linear stability of the uniform flow state on a wetting stripe in the framework of continuum fluid mechanics. For simplicity we consider stripes of infinite length in order to avoid the problem of wavelength selection. Assuming the liquid is Newtonian and incompressible, its flow velocity $\mathbf{u} = u\mathbf{e}_r + v\mathbf{e}_\phi + w\mathbf{e}_z$ for the geometry shown in Fig. 1 is governed by the Navier-Stokes equation

$$\frac{\partial \mathbf{u}}{\partial t} + \mathbf{u} \cdot \nabla \mathbf{u} = -\frac{1}{\rho} \nabla p + \frac{\eta}{\rho} \nabla^2 \mathbf{u} + g\mathbf{e}_z \quad (4)$$

and the incompressibility condition $\nabla \cdot \mathbf{u} = 0$, where ρ and p are the mass density and the pressure, respectively. In addition, the deformation of the free surface $R(\phi, z, t)$ is described by the kinematic condition

$$\frac{\partial R}{\partial t} + \frac{v}{R} \frac{\partial R}{\partial \phi} + w \frac{\partial R}{\partial z} = u, \quad (5)$$

which expresses the fact that (for a non-volatile liquid) a fluid particle at the interface moves inwards or outwards with the interfacial velocity. At the impermeable solid, \mathbf{u} satisfies the no-slip boundary condition (which is consistent

with the MD simulations). At the free surface, assuming that the liquid is non-volatile, the appropriate boundary conditions are the balance of the normal component of the stress $\mathbf{n} \cdot (\mathbf{T} \cdot \mathbf{n}) = -\gamma\kappa$, and the condition of zero tangential force, $\mathbf{t} \cdot (\mathbf{T} \cdot \mathbf{n}) = 0$. Here κ is the local mean curvature of the liquid-vapor interface, $\mathbf{T} = -p\mathbf{I} + \eta[(\nabla\mathbf{u}) + (\nabla\mathbf{u})^T]$ is the stress tensor, \mathbf{n} is the unit normal vector pointing towards the vapor phase, and \mathbf{t} with $\mathbf{n} \cdot \mathbf{t} = 0$ is any unit tangent vector on the surface. Since we are considering a non-volatile liquid, we can assume that the density, the viscosity, and the pressure of the vapor phase are negligible.

Referring to Fig. 1, we assume that surface tension and substrate potential act – for a sufficiently large liquid volume – to pin the liquid at the edges of the wetting stripe, and to fix the initial liquid-vapor interface to be a (constant-curvature) section of a circular cylinder. The contact angle at the edge of the liquid can then take on any value between that corresponding to the wetting region on the stripe (0°) and that to the non-wetting one on the exterior (180°). For any given constant initial height h_0 and acceleration g , Eq. (4) has a steady-state unidirectional flow solution $\mathbf{u} = w_0(r, \phi) \mathbf{e}_z$ which satisfies the two-dimensional Poisson equation

$$\frac{1}{r} \frac{\partial}{\partial r} \left(r \frac{\partial w_0}{\partial r} \right) + \frac{1}{r^2} \frac{\partial^2 w_0}{\partial \phi^2} = -\frac{\rho g}{\eta}. \quad (6)$$

The boundary conditions for \mathbf{u} reduce to $w_0 = 0$ at the substrate ($|x| \leq a, y = 0$) and $\partial w_0 / \partial n = 0$ at the free surface ($r = R, y > 0$). The axially constrained shape of the initial liquid-vapor interface can be written as

$$R(\phi, z, t) \rightarrow R_0(\phi) = a(b_0 \sin \phi + \sqrt{1 + b_0^2 \sin^2 \phi}) \quad (7)$$

with

$$b_0 = \frac{1}{2} \left(\frac{h_0}{a} - \frac{a}{h_0} \right). \quad (8)$$

The pressure inside the liquid is $p_0 = \gamma/R_c$ where $R_c = (h_0^2 + a^2)/(2h_0)$ is the radius of the truncated cylinder. For general h_0/a , we obtain the base state w_0 by solving Eq. (6) numerically, using a finite difference discretization. In the special case in which the liquid occupies exactly half of a circular cylinder (i.e., $h_0/a = 1$), one can obtain an explicit Fourier series solution with the separation ansatz $w_0(r, \phi) = -\rho g r^2 / (4\eta) + B_0 + \sum_{n=1}^{\infty} r^n [A_n \sin(n\phi) + B_n \cos(n\phi)]$. The boundary conditions and the symmetry of $w_0(r, \phi)$ determine the coefficients A_n and B_n , and we obtain

$$w_0(r, \phi) = \frac{\rho g a^2}{\eta} \left[\frac{1}{4} \left(\frac{r}{a} \right)^2 (\cos 2\phi - 1) - \sum_{n=1,3,5,\dots} \frac{8}{\pi n^2 (n^2 - 4)} \left(\frac{r}{a} \right)^n \sin n\phi \right], \quad (9)$$

which has been discussed in Sec. II and is plotted as the NS velocity in Fig. 3.

If the liquid starts from rest, the time scale for the steady state to develop is controlled by the diffusion of vorticity, which happens in the cases simulated above on the time scale $\tau_D = \rho a^2 / \eta \approx 6 - 16 \tau$, which is much smaller than the characteristic time for the long wavelength instability to appear. It is reasonable, therefore, to study the stability of the flowing liquid ridge by investigating a small perturbation about the basic unidirectional steady state. Hence, we write $\mathbf{u} = u' \mathbf{e}_r + v' \mathbf{e}_\phi + (w_0 + w') \mathbf{e}_z$, $p = p_0 + p'$ and $R = R_0(\phi) + R'(\phi, z, t)$ and linearize Eqs. (4), (5), and all the necessary boundary conditions about the basic state. This leads to a set of linear partial differential equations (PDE) for the small quantities u' , v' , w' , p' and R' . The results are [19]:

$$\frac{\partial u'}{\partial t} = -\frac{1}{\rho} \frac{\partial p'}{\partial r} + \frac{\eta}{\rho} \left(\nabla^2 u' - \frac{u'}{r^2} - \frac{2}{r^2} \frac{\partial v'}{\partial \phi} \right) - w_0 \frac{\partial u'}{\partial z} \quad (10)$$

$$\frac{\partial v'}{\partial t} = -\frac{1}{\rho r} \frac{\partial p'}{\partial \phi} + \frac{\eta}{\rho} \left(\nabla^2 v' - \frac{v'}{r^2} + \frac{2}{r^2} \frac{\partial u'}{\partial \phi} \right) - w_0 \frac{\partial v'}{\partial z} \quad (11)$$

$$\frac{\partial w'}{\partial t} = -\frac{1}{\rho} \frac{\partial p'}{\partial z} + \frac{\eta}{\rho} \nabla^2 w' - w_0 \frac{\partial w'}{\partial z} \quad (12)$$

for the velocity and

$$\frac{\partial R'}{\partial t} = u' - \frac{v'}{R_0} \frac{\partial R_0}{\partial \phi} - w_0 \frac{\partial R'}{\partial z} \quad (13)$$

for the kinematic condition in Eq. (5). At any time t , p' satisfies the pressure equation

$$\nabla^2 p' = -2\rho \left(\frac{\partial w_0}{\partial r} \frac{\partial u'}{\partial z} + \frac{1}{r} \frac{\partial w_0}{\partial \phi} \frac{\partial v'}{\partial z} \right), \quad (14)$$

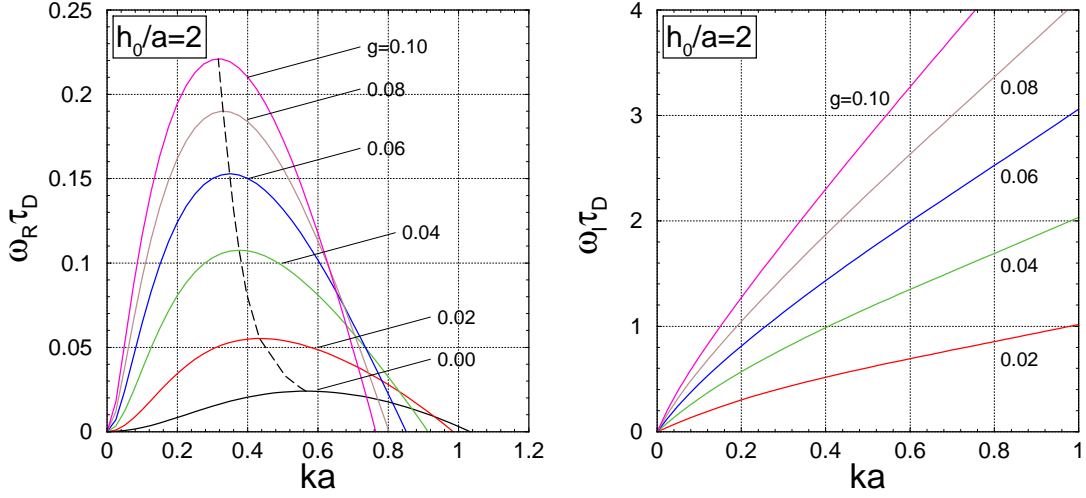


FIG. 10: Real (left) and imaginary (right) parts of the growth rate $\omega(k, 1)$ (in units of $\tau_D = \rho a^2 / \eta$) of the dominant growing instability modes as function of the wavenumber k of the perturbation and for $n = 1$ (see Eq. (22)) for a liquid ridge with $h_0/a = 2.0$. The wavelength of the fastest growing mode and the corresponding growth rate increase with g . The dashed line marks the loci of these maxima as g varies from $g = 0$ to 0.1 from bottom to top. The accelerations g are measured in units of $\sigma \tau^{-2}$. Note that $\omega_R(k > k_{\max}(g)) < 0$, which implies that perturbations with shorter wavelengths are linearly stable. Stronger forcing leads to faster growth of the most unstable perturbation but in the same time leads to a stabilization of perturbations with shorter wavelengths.

which is obtained by taking the divergence of Eq. (4) and using the incompressibility condition.

The velocity boundary conditions, upon evaluation at the liquid-vapor interface position $r = R_0(\phi) + R'(\phi, z, t)$ and after linearization, are:

$$\frac{\partial u'}{\partial z} + \frac{\partial w'}{\partial r} - \frac{R_{0\phi}}{R_0} \left(\frac{\partial v'}{\partial z} + \frac{1}{R_0} \frac{\partial w'}{\partial \phi} \right) - \frac{1}{R_0^2} \frac{\partial w_0}{\partial \phi} \left(R'_\phi - \frac{2R_{0\phi}}{R_0} R' \right) + \left(\frac{\partial^2 w_0}{\partial r^2} - \frac{R_{0\phi}}{R_0^2} \frac{\partial^2 w_0}{\partial r \partial \phi} \right) R' = 0 \quad (15)$$

from $\mathbf{t}_z \cdot (\mathbf{T} \cdot \mathbf{n}) = 0$;

$$\left(1 - \frac{R_{0\phi}^2}{R_0^2} \right) \left[\frac{\partial v'}{\partial r} - \frac{1}{R_0} \left(v' - \frac{\partial u'}{\partial \phi} \right) \right] + \frac{2R_{0\phi}}{R_0} \left(2 \frac{\partial u'}{\partial r} + \frac{\partial w'}{\partial z} \right) - \frac{1}{R_0} \left(1 + \frac{R_{0\phi}^2}{R_0^2} \right) \frac{\partial w_0}{\partial \phi} R'_z = 0 \quad (16)$$

from $\mathbf{t}_\phi \cdot (\mathbf{T} \cdot \mathbf{n}) = 0$; and

$$\frac{\partial u'}{\partial r} = -\frac{1}{R_0} \left(u' + \frac{\partial v'}{\partial \phi} \right) - \frac{\partial w'}{\partial z} \quad (17)$$

from $\nabla \cdot \mathbf{u} = 0$. The no-slip boundary condition at the substrate requires $u' = v' = w' = 0$ at $\phi = 0$ and $\phi = \pi$.

Applying the normal stress condition at the liquid-vapor interface $r = R_0(\phi) + R'(\phi, z, t)$ gives

$$\begin{aligned} p' = & -\frac{\gamma R'_{zz}}{(1 + R_{0\phi}^2/R_0^2)^{1/2}} \\ & -\frac{\gamma}{R_0^2(1 + R_{0\phi}^2/R_0^2)^{3/2}} \left\{ R'_\phi - \left[\frac{R_{0\phi\phi}}{R_0} - \frac{4R_{0\phi}^2}{R_0^2} - \left(\frac{1 - 2R_{0\phi}^2/R_0^2}{1 + R_{0\phi}^2/R_0^2} \right) \left(1 + \frac{2R_{0\phi}^2}{R_0^2} - \frac{R_{0\phi\phi}}{R_0} \right) \right] R' \right. \\ & \left. - \frac{R_{0\phi}}{R_0} \left(\frac{1 - 2R_{0\phi}^2/R_0^2 + 3R_{0\phi\phi}/R_0}{1 + R_{0\phi}^2/R_0^2} \right) R'_\phi \right\} \\ & + \frac{2\eta}{(1 + R_{0\phi}^2/R_0^2)} \left[\frac{\partial u'}{\partial r} - \frac{R_{0\phi}}{R_0} \left(\frac{\partial v'}{\partial r} - \frac{v'}{R_0} + \frac{1}{R_0} \frac{\partial u'}{\partial \phi} \right) + \frac{R_{0\phi}^2}{R_0^3} \left(u' + \frac{\partial v'}{\partial \phi} \right) \right] \end{aligned} \quad (18)$$

after linearization. In Eqs. (15), (16), and (18), the subscript ϕ denotes differentiation with respect to ϕ , and $r = R_0(\phi)$.

We have solved the linearized equations using the pressure Poisson equation (PPE) formulation [20, 21], which requires boundary conditions for the pressure p' at the substrate. These conditions can be obtained from the projections of Eq. (4) along \mathbf{n} and \mathbf{t} , and from the incompressibility condition. To linear order, they become

$$\frac{1}{r} \frac{\partial p'}{\partial \phi} = \eta \left(\nabla^2 v' + \frac{2}{r^2} \frac{\partial u'}{\partial \phi} \right), \quad (19)$$

$$\frac{\partial p'}{\partial r} = \eta \left(\nabla^2 u' - \frac{2}{r^2} \frac{\partial v'}{\partial \phi} \right), \quad (20)$$

and

$$\frac{1}{r} \frac{\partial (ru')}{\partial r} + \frac{1}{r} \frac{\partial v'}{\partial \phi} + \frac{\partial w'}{\partial z} = 0 \quad (21)$$

at $\phi = 0$ or π .

We represent the small quantities in terms of Fourier series expansions, and finally derive a set of evolution equations for the Fourier components. In this way, we reduce the three-dimensional problem to a set of two-dimensional linear PDEs for each Fourier mode, characterized by a wavenumber k . We consider a small initial sinusoidal perturbation of the liquid-vapor interface of the form $R'(\phi, z, t = 0) = \epsilon \cos kz \sin \phi$ for $|\epsilon| \ll R_0$, and follow its evolution by solving the initial value problem numerically. The solution is expanded in a Fourier series of the form

$$R'(\phi, z, t) = \sum_{n=1}^{\infty} \int dk A_{nk}(t) e^{-ikz} \sin n\phi, \quad (22)$$

and the real and imaginary parts of the dominant growth rate $\omega(k, n) = \omega_R(k, n) + i\omega_I(k, n)$ are extracted from the time-dependent amplitude $A_{nk}(t) \propto e^{\omega(k, n)t}$. Modes with $n > 1$ are stable. The functions $\omega(k, 1)$ for the case $h_0/a = 2$ at different values of g are shown in Fig. 10. It is evident from Fig. 10 that both the amplitude growth rate ω_R and the phase velocity ω_I/k increase as g increases, which is consistent with the MD simulations. The slight change in wavelength of the maximally unstable mode between $g = 0.01$ and $g = 0.025$, which are the values used in the MD simulations, could not be detected in the simulations for the reasons discussed in Sec. II. We have carried out the same calculation also for the case $h_0/a = 4$ and the results are qualitatively the same. For the case $h_0/a = 1$, all Fourier modes are stable.

V. LONG-WAVELENGTH APPROXIMATION

Since the initial liquid configuration is a long ridge with a uniform cross section, and the structures which develop have, at least initially, characteristic length scales much larger than the width of the ridge, it is natural to consider a long-wavelength approximation to the Navier-Stokes equation. Referring to Fig. 1, incompressibility implies the continuity equation

$$\frac{\partial A}{\partial t} = -\frac{\partial Q}{\partial z} \quad (23)$$

where A is the local cross-sectional area

$$A(z, t) = \frac{1}{2} \int_0^\pi d\phi R^2(\phi, z, t) \quad (24)$$

and Q is the volumetric flow rate given by

$$Q(z, t) = \int_0^\pi d\phi \int_0^{R(\phi, z, t)} dr r w(r, \phi, z, t) \quad (25)$$

with $w(r, \phi, z, t)$ being the axial component of the flow velocity.

If we assume that the local cross section always has a circular boundary, the free surface can be described by Eq. (7) with $b = b(z, t)$ expressed in terms of the local height $h = h(z, t)$ according to the same functional relation as between the initial value b_0 and the initial height h_0 , Eq. (8). In this case, the integral in Eq. (24) yields

$$A = a^2 \left[b + (1 + b^2) \left(\frac{\pi}{2} + \arctan b \right) \right], \quad (26)$$

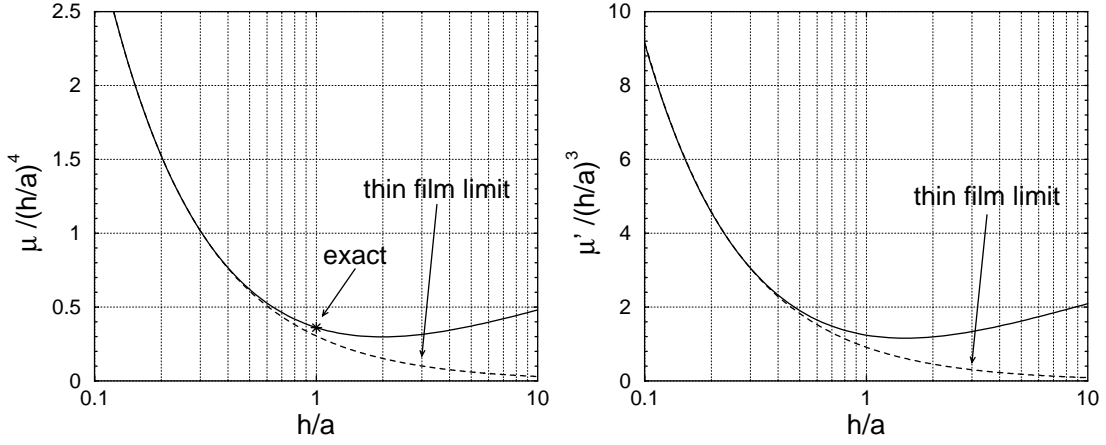


FIG. 11: The mobility $\mu(h/a)$ as defined in Eq. (30) in units of $(h/a)^4$ (left) and its derivative in units of $(h/a)^3$ (right) from a numerical solution of the Stokes equation. The dashed lines correspond to the thin film limit $h/a \rightarrow 0$. The value of $\mu(1)$ is known exactly. These units are chosen as to make the difference between the numerical solutions and the thin film limit particularly visible. Moreover, it is the combination $a^4 \mu(h/a)$ which enters into Eq. (30) for the flux Q .

so that

$$\frac{\partial A}{\partial t} = a \left(1 + \frac{a^2}{h^2} \right) \left[1 + b \left(\frac{\pi}{2} + \arctan b \right) \right] \frac{\partial h}{\partial t}. \quad (27)$$

Instead of performing a systematic long wavelength expansion we further assume that $w(r, \phi, z, t)$ can be approximated by the steady state axial flow field of a liquid ridge with uniform cross-sectional shape given by the local profile $R(\phi, z, t)$. The flow is driven by the effective forcing $(g - \frac{1}{\rho} \frac{\partial p}{\partial z})$, which means that $w(r, \phi, z, t)$ is given by the solution of Eq. (6) with $\frac{\rho g}{\eta}$ replaced by $(\frac{\rho g}{\eta} - \frac{1}{\eta} \frac{\partial p}{\partial z})$. This allows for the ansatz

$$w(r, \phi, z, t) = w_1(r, \phi; z, t) \left(\frac{\rho g}{\eta} - \frac{1}{\eta} \frac{\partial p}{\partial z} \right) \quad (28)$$

due to the linearity of the Poisson equation. Here w_1 has the dimension of an area and is proportional to the base state velocity w_0 of the previous section because it obeys the same boundary conditions. Note that although w_1 is proportional to the velocity in a uniform infinite ridge, a function of r and ϕ , it depends implicitly on z and t because of the boundary conditions imposed at $r = R(\phi, z, t)$. The Laplace pressure p in Eq. (28) is approximately given by

$$p = \gamma \kappa \approx \gamma \left(\frac{2h}{h^2 + a^2} - \frac{\partial^2 h}{\partial z^2} \right), \quad (29)$$

where the first term $2h/(h^2 + a^2)$ is the inverse radius of curvature of the local circular cross-section set by the local height h , and the second is the (leading order approximation to) the curvature in the orthogonal plane. Within this approximation the flux is

$$Q = \left[\int_0^\pi d\phi \int_0^{R_0(\phi)} dr r w_1(r, \phi; z, t) \right] \left(\frac{\rho g}{\eta} - \frac{1}{\eta} \frac{\partial p}{\partial z} \right) \equiv \frac{a^4}{\eta} \mu \left(\frac{h}{a} \right) \left(\rho g - \frac{\partial p}{\partial z} \right). \quad (30)$$

Since w_1 is proportional to w_0 , the solution for w_1 can be inferred from Sec. IV and in general it is obtained numerically. The dimensionless ‘‘mobility’’ $\mu(h/a)$ (i.e., the proportionality factor between the flux-driving pressure gradient and the flow rate), defined via Eq. (30), is obtained by numerical integration of the solution of Eq. (6). In Sec. II we considered the special case $h/a = 1$, for which Eq. (9) provides the analytical solution, which in turns gives $\mu(1) = \frac{1}{4} \left\{ \frac{1}{\pi} [6 + 7\zeta(3)] - \pi \right\} = 0.362$. The thin film limit $h/a \rightarrow 0$ is an interesting special case as well. In this limit, we have a Poiseuille velocity profile locally and therefore $w_1 = w_1(x, y) = \ell(x)y - \frac{1}{2}y^2$ where $\ell(x) = h [1 - (x/a)^2]$ is the local film height as a function of the lateral position x . This leads to $\mu(h/a \rightarrow 0) = \frac{32}{105} (h/a)^3$. Figure 11 shows the mobility μ and its derivative as functions of h/a together with their limiting behaviors for $h/a \rightarrow 0$.

With Eqs. (27) and (30), the continuity equation (23) can be re-written as

$$\left(1 + \frac{a^2}{h^2} \right) \left[1 + b \left(\frac{\pi}{2} + \arctan b \right) \right] \frac{\partial h}{\partial t} = \frac{a^3}{\eta} \left[\mu \left(\frac{h}{a} \right) \frac{\partial^2 p}{\partial z^2} - \frac{1}{a} \mu' \left(\frac{h}{a} \right) \left(\rho g - \frac{\partial p}{\partial z} \right) \frac{\partial h}{\partial z} \right]. \quad (31)$$

Denoting the local height by $h = h_0 + \delta h(z, t)$ and linearizing Eq. (31) around h_0 gives

$$\left(1 + \frac{a^2}{h_0^2}\right) \left[1 + b_0 \left(\frac{\pi}{2} + \arctan b_0\right)\right] \frac{\partial \delta h}{\partial t} = -\frac{\gamma a^3}{\eta} \mu\left(\frac{h_0}{a}\right) \left[\frac{2(h_0^2 - a^2)}{(h_0^2 + a^2)^2} \frac{\partial^2 \delta h}{\partial z^2} + \frac{\partial^4 \delta h}{\partial z^4}\right] - \frac{\rho g a^2}{\eta} \mu'\left(\frac{h_0}{a}\right) \frac{\partial \delta h}{\partial z} \quad (32)$$

with $b_0 = (h_0/a - a/h_0)/2$. Specializing now to a sinusoidal perturbation $\delta h \sim e^{\omega t - i k z}$ yields

$$\left(1 + \frac{a^2}{h_0^2}\right) \left[1 + b_0 \left(\frac{\pi}{2} + \arctan b_0\right)\right] \omega = \frac{\gamma a^3}{\eta} \mu\left(\frac{h_0}{a}\right) \left[\frac{2(h_0^2 - a^2)}{(h_0^2 + a^2)^2} k^2 - k^4\right] + i \frac{\rho g a^2}{\eta} \mu'\left(\frac{h_0}{a}\right) k. \quad (33)$$

From this, one can identify the real and imaginary parts of the growth rate ω :

$$\omega_R = \frac{\gamma}{\eta a} \mu\left(\frac{h_0}{a}\right) \left(1 + \frac{a^2}{h_0^2}\right)^{-1} \left[1 + b_0 \left(\frac{\pi}{2} + \arctan b_0\right)\right]^{-1} \left[\frac{2(h_0^2/a^2 - 1)}{(h_0^2/a^2 + 1)^2} (k a)^2 - (k a)^4\right] \quad (34)$$

$$\omega_I = \frac{\rho g a}{\eta} \mu'\left(\frac{h_0}{a}\right) \left(1 + \frac{a^2}{h_0^2}\right)^{-1} \left[1 + b_0 \left(\frac{\pi}{2} + \arctan b_0\right)\right]^{-1} (k a). \quad (35)$$

Graphs of ω_R for the two cases simulated by MD are shown in Fig. 12. Equation (34) shows that a long wavelength perturbation to a liquid ridge of uniform height is unstable for $h_0 > a$ (i.e., for contact angles larger than 90°) and is stable otherwise. Figure 12 indicates that for thick ridges the instability grows more rapidly but only for longer wavelengths. Equation (35) shows that the phase velocity ω_I/k is proportional to the acceleration g , which is consistent with the observation in MD that stronger forcing leads to faster moving pearls. However, within this simple approach, the amplitude growth rate ω_R is independent of g opposite to what is observed in the MD simulations and predicted by the stability analysis in Sec. IV. Numerical values for the growth rate, the critical wavelength, and the phase velocity are compared with the simulation results in Table I, showing at least qualitative agreement.

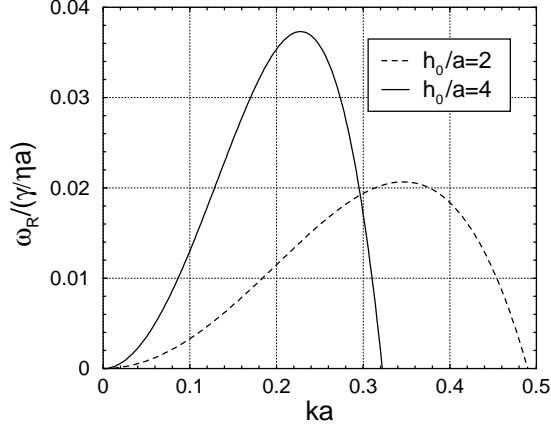


FIG. 12: The real part of the growth rate of unstable modes for two values of h_0/a in the long-wavelength approximation (see Eq. (34)). In contrast to the full linear stability analysis in Sec. IV, the real part does not depend on g . ω_R is negative for $h_0/a < 1$.

VI. SUMMARY AND DISCUSSION

Motivated by possible applications in the field of open microfluidic systems we have studied the flow of a non-volatile liquid ridge along a stripe-like chemical channel, to which the liquid is confined by wettability (see Fig. 1). In this context the most salient question concerns stability, i.e., the degree to which the liquid remains on the channel and the effects of any changes in the shape of the liquid-vapor interface. Our basic tool to calculate the flow has been large scale molecular dynamics simulations, which directly incorporate the molecular interactions underlying the wettability contrast on the flat substrate (see Fig. 2 for a snapshot). A number of different cases were considered (see Fig. 4) which varied the amount of liquid present atop the stripe and the wettability of the exterior region. In order to

understand the numerical results, we have carried out a systematic linear stability analysis of the corresponding free boundary problem for the incompressible Navier-Stokes equation and find qualitative agreement. In addition to the full stability analysis we have presented a much simpler long-wavelength approximation for channel flow on straight chemical channels, which is able to capture some but not all of the qualitative features of the flow.

The basic liquid configuration at rest, i.e., a non-volatile ridge of uniform cross-sectional shape, is known to be unstable due to a surface tension driven instability, similar to the Rayleigh-Plateau instability, if the contact angle is larger than 90° (see Fig. 5). The MD simulations show that when the liquid is driven along the channel, the instability is enhanced by the driving if it is also present in the non-driven case (compare the times in Fig. 5 to those in Figs. 6 and Fig. 7). However, statically stable liquid ridges are not destabilized by the flow. In the unstable case a periodic string of pearls appears growing in amplitude while propagating along the ridge. At later times, when nonlinear effects are manifest, the pearls develop distinct velocities and merge into pairs until only one of them survives. Despite substantial changes in amplitude and shape, the pearls remain confined to the chemical channel up to rather high accelerations. The instability has a beneficial side effect, in that the throughput is enhanced as compared to the homogeneously filled case (see Fig. 9). For very high accelerations, however, the pearls are heavily deformed and in some cases lose contact with the substrate. A somewhat surprising result is that when the solid exterior to the wetting stripe is partially wetting rather than completely non-wetting, the qualitative behavior is unchanged (see Fig. 8) and the liquid remains atop the stripe.

The wavelength of the pearling instability is reasonably well predicted by a full linear stability analysis of the Stokes free boundary problem (see Fig. 10 for the dispersion relations of the most unstable modes). For the accelerations studied in the MD simulations, the change in the wavelength of the most unstable mode as compared to the corresponding static case is too small to be detectable in MD simulations. However, the growth rate of the most unstable mode increases significantly upon forcing, in qualitative agreement with the MD simulations. The results are summarized in Tab. I. A precise comparison between the MD results and the stability calculations is hampered by the thermal fluctuations present in the molecular simulation, which are exacerbated by the presence of a free surface which appears as a broad interfacial region (see Fig. 3). As a result, it is difficult to identify from the simulations the individual modes of the stability analysis, and their growth rates cannot be measured directly.

The onset of the instability at contact angle 90° as well as the wavelength of the instability are reasonably well predicted by a simple long-wavelength expansion of the Stokes free boundary problem. Within this approximation, the only non-trivial part of the calculation is the numerical determination of the mobility (see Fig. 11). However, since the most unstable wavelength is of the order of the ridge diameter, only qualitative results can be expected. In contrast to the MD results as well as to the full stability analysis, within this approximation the maximally unstable wavelength turns out to be independent of the acceleration (see Fig. 12 for the real part of the dispersion relation).

The agreement between the MD simulation results and hydrodynamics (see Fig. 3) is less satisfactory than in other geometries without a free surface. The main reason seems to be the presence of thermal fluctuations of the liquid-vapor interface, i.e., capillary wave-like excitations, which broaden the liquid-vapor interface. The incorporation of thermal fluctuations has proven successful in relating MD simulations of a free liquid jet to the NS equations [22], and more recently, have been included in a hydrodynamic thin film model [23, 24]. An extension of this technique to liquid ridges with large contact angles in chemical channels might improve the agreement with the simulations.

Another possible source of disagreement between the MD simulations and the NS results is the neglect of the disjoining pressure in the hydrodynamic calculations. The issue arises because large portions of *thin* liquid films are exposed to the long-ranged substrate potentials and to the absence of liquid molecules outside the films [25, 26], and is expected to be important in the nanoscale flows studied here. In the simple case of a film of nearly constant thickness atop an infinite homogeneous substrate, the effect of the disjoining pressure is captured by adding a contribution $-A_H/h^3$ to the pressure, where A_H is the Hamaker constant, which is positive in a completely wetting case. If we repeat the long-wavelength analysis with this additional term added to the right hand side of Eq. (29), the effect of the disjoining pressure is to modify the amplitude growth rate to

$$\omega_R = \frac{\gamma}{\eta a} \mu \left(\frac{h_0}{a} \right) \left(1 + \frac{a^2}{h_0^2} \right)^{-1} \left[1 + b_0 \left(\frac{\pi}{2} + \arctan b_0 \right) \right]^{-1} \left\{ \left[\frac{2(h_0^2/a^2 - 1)}{(h_0^2/a^2 + 1)^2} - \frac{3A_H}{\gamma a^2} \left(\frac{a}{h_0} \right)^4 \right] (ka)^2 - (ka)^4 \right\},$$

Hence, the disjoining pressure has a stabilizing effect. It lowers the maximum growth rate and shifts the most unstable mode towards longer wavelength. In terms of the stability criterion, it leads to $h_0 > a \left[1 + \frac{3A_H}{2\gamma a^2} \left(1 + \frac{a^2}{h_0^2} \right)^2 \right]^{1/2}$ instead of $h_0 > a$. For realistic values of A_H [26], we get $3A_H/2\gamma a^2 \sim 10^{-1}$. Such a difference will be masked by the uncertainties in MD simulations due to thermal noise and is undetectable at the present level of accuracy of our results. This calculation is only approximate, since the geometry in this paper is rather more complicated than a

nearly-uniform film on a homogeneous substrate. Other authors have extended this disjoining pressure analysis to the wedge-shaped geometries arising in drop spreading [27, 28, 29], and to substrates with heterogeneous chemical patterns [30, 31, 32], but we feel that dealing with the other effects noted above is more pressing. Note that the MD simulations did not include a *long*-ranged disjoining pressure contribution per se, since the LJ interaction is cut off. The reason is that in MD simulations of flow at the 10 nm scale, the principal effect arises from the short-ranged interactions between liquid and solid atoms, and the long-ranged tail has a negligible effect (see, e.g., Ref. [13]).

For wetting *transitions* however, this tail is quite important [25]. In particular on chemically structured surfaces, the influence of the laterally inhomogeneous substrate potential on the wetting film thickness has been discussed in detail [29, 30] and on chemical stripes morphological phase transitions have been predicted [31, 32]. Recent experiments have confirmed the theoretical predictions on the structure of wetting films on a chemical stripe [33]. However, the thermodynamical ensemble plays a crucial role here. There are three types of ensembles which have to be distinguished due to their distinct characters. If the substrate is exposed to a large vapor reservoir one deals with a grand canonical ensemble as studied theoretically in Refs. [29, 30, 31, 32] and experimentally in Ref. [33]. For a volatile liquid enclosed into an isolating container one has a canonical ensemble; the MD simulations presented here correspond to this case. For a completely non-volatile liquid the liquid volume in the ridge is strictly conserved; this case has been studied in Refs. [8, 9] and corresponds to the situation considered for the analytic hydrodynamic analyses in Sects. IV and V. The MD simulations are well described by the non-volatile Stokes dynamics, because the vapor pressure is very low and the vapor volume is small. Instabilities, such as the pearling instability, cannot be observed in a grand canonical setting (in accordance with the experimental observations in Ref. [33]), because they only occur in situations in which the pressure in the liquid ridge decreases with increasing volume. In this case, in a grand canonical setting, however, more and more molecules would be drawn out of the reservoir onto the ridge and it would grow without limit. Interestingly, the authors of Ref. [33] find that the disjoining pressure does not influence the ridge shape above a ridge height of approximately 8 nm. This finding corroborates our conjecture given above, that the influence of the substrate potential on the instability studied in the present paper is small.

In this work we have considered inertial driving, i.e., a force acting on every liquid atom in the system independent of its distance from the substrate surface. Although the physical mechanism for driving the liquid is qualitatively different, we expect electro-osmotically driven liquids to behave very similarly, in particular for low ion concentrations. If in such systems the Debye layer thickness is on the order of the ridge diameter, the ions are almost homogeneously distributed inside the ridge and the electrical force acts equally everywhere. This is in contrast to macroscopic systems, where the Debye layer is thin as compared to the system size and the electrical force only acts at the boundary of the system.

Since the pearling instability increases the flow through a chemical channel (see Fig. 9), it might be an advantage to operate a microfluidic system in the unstable regime. Moreover, since the initially formed pearls have a relatively narrow size distribution, a chemical channel could be used as a nano-droplet dispenser. For longitudinal driving, the liquid stays on the chemical stripe even at high accelerations and when the instability is fully developed. For applications the stability with respect to non-longitudinal driving as well as the behavior at junctions and bends will be important. Full three-dimensional Stokes flow simulations, possibly taking into account the effect of long-ranged interactions and thermal fluctuations, should be used in order to interpret the results of MD simulations in such complicated geometries.

Acknowledgments

JK and TSL are supported in part by the NASA Explorations Systems Mission Directorate. Computational resources were provided by the Rechenzentrum Garching der Max-Planck-Gesellschaft und des Instituts für Plasma-physik.

-
- [1] N. Giordano and J.-T. Cheng, “Microfluidic mechanics: progress and opportunities”, *J. Phys.: Condens. Matter* **13**, R271 (2001).
 - [2] P. Mitchell, “Microfluidics – downsizing large-scale biology”, *Nature Biotech.* **19**, 717 (2001).
 - [3] H. A. Stone and S. Kim, “Microfluidics: Basic issues, applications, and challenges”, *AIChE J.* **47**, 1250 (2001).
 - [4] A. A. Darhuber, S. M. Troian, and W. W. Reisner, “Dynamics of capillary spreading along hydrophilic microstrips”, *Phys. Rev. E* **64**, 031603 (2001).
 - [5] H. Gau, S. Herminghaus, P. Lenz, and R. Lipowsky, “Liquid morphologies on structured surfaces: From microchannels to microchips”, *Science* **283**, 46 (1999).
 - [6] S. Dietrich, M. N. Popescu, M. Rauscher, “Wetting on structured substrates”, *J. Phys.: Condens. Mat.* **17**, S577 (2005).

- [7] S. H. Davis, “Moving contact line and rivulet instabilities. Part 1: The static rivulet”, *J. Fluid Mech.* **98**, 225 (1980).
- [8] M. Brinkmann, J. Kierfeld, and R. Lipowsky, “Stability of liquid channels or filaments in the presence of line tension”, *J. Phys.: Condens. Mat.* **17**, 2349 (2005).
- [9] M. Brinkmann and R. Lipowsky, “Wetting morphologies on substrates with striped surface domains”, *J. Appl. Phys.* **92**, 4296 (2002).
- [10] M. P. Allen and D. J. Tildesley, *Computer Simulation of Liquids* (Clarendon Press, Oxford, 1987).
- [11] D. Frenkel and B. Smit, *Understanding Molecular Simulation*, 2nd ed. (Academic Press, San Diego, 2002).
- [12] J. Koplik and J. R. Banavar, “Continuum deductions from molecular hydrodynamics”, *Annu. Rev. Fluid Mech.* **27**, 257 (1995).
- [13] J. Koplik and J. R. Banavar, “Molecular simulation of dewetting”, *Phys. Rev. Lett.* **84**, 4401 (2000).
- [14] G. S. Grest and K. Kremer, “Molecular dynamics simulation for polymers in the presence of a heat bath,” *Phys. Rev. A* **33**, 3628 (1986).
- [15] A. A. Darhuber, S. M. Troian and S. M. Miller, “Morphology of liquid microstructures on chemically patterned surfaces”, *J. Appl. Phys.* **87**, 7768 (2000).
- [16] J. Koplik and J. R. Banavar, “Molecular dynamics of interface rupture”, *Phys. Fluids A* **5**, 521 (1993).
- [17] S. Kawano, “Molecular dynamics of rupture phenomena in a liquid thread”, *Phys. Rev. E* **58**, 4468 (1998).
- [18] K. Kadau, T. C. Germann, N. C. Hadjiconstantinou, P. S. Lomdahl, G. Dimonte, B. L. Holian, and B. J. Alder, “Nanohydrodynamics simulations: an atomistic view of the Rayleigh-Taylor instability,” *Proc. Natl. Acad. Sci. (US)* **101**, 5851 (2004).
- [19] G. K. Batchelor, *An Introduction to Fluid Dynamics* (Cambridge University Press, Cambridge, 1967), Appendix 2.
- [20] P. M. Gresho and R. L. Sani, “On pressure boundary conditions for the incompressible Navier-Stokes equations”, *Int. J. Numer. Methods Fluids* **7**, 1111 (1987).
- [21] H. Johnston and J.-G. Liu, “Finite difference schemes for incompressible flow based on local pressure boundary conditions”, *J. Comput. Phys.* **180**, 120 (2002).
- [22] M. Moseler and U. Landman, “Formation, stability and breakup of nanojets,” *Science* **289**, 1165 (2000).
- [23] G. Grün, K. Mecke, and M. Rauscher, “Thin-film flow influenced by thermal noise”, submitted to *J. Stat. Phys.* (2005).
- [24] B. Davidovich, E. Moro, and H. A. Stone, “Spreading of thin films assisted by thermal fluctuations,” preprint cond-mat/0509803 (2005).
- [25] S. Dietrich, “Wetting Phenomena,” in *Phase Transitions and Critical Phenomena*, vol. 12, ed. C. Domb and J. L. Lebowitz (Academic Press, London, 1988), p. 1.
- [26] J. N. Israelachvili, *Intermolecular and Surface Forces*, 2nd Ed., (Academic Press, London, 1992).
- [27] L. M. Hocking, “The influence of intermolecular forces on thin fluid layers,” *Phys. Fluids* **5**, 793 (1993).
- [28] Q. Wu and H. Wong, “A slope-dependent disjoining pressure for non-zero contact angles,” *J. Fluid Mech.* **506**, 157 (2004).
- [29] C. Bauer and S. Dietrich, “Quantitative study of lateral inhomogeneous wetting films”, *Eur. Phys. J. B* **10**, 767 (1999).
- [30] C. Bauer and S. Dietrich, “Wetting films on chemically heterogeneous surfaces,” *Phys. Rev. E* **60**, 6919 (1999).
- [31] C. Bauer, S. Dietrich, and A. O. Parry, “Morphological phase transitions of thin fluid films on chemically structured substrates”, *Europhys. Lett.* **47**, 474 (1999).
- [32] C. Bauer and S. Dietrich “Phase diagram for morphological transitions of wetting films on chemically structured substrates,” *Phys. Rev. E* **61**, 1664 (2000).
- [33] A. Checco, O. Gang, and B. M. Ocko, “Liquid nanostripes”, private communication.